AIMS Materials Science, 13(1): 120–140.
DOI: 10.3934/matersci.2026007
Received: 13 November 2025
Revised: 31 December 2025
Accepted: 14 January 2026
Published: 26 January 2026

https://www.aimspress.com/journal/Materials

Research article

Enhancing corrosion resistance of anodized aluminum alloy 6061 via multicomponent silica sol-gel sealing

Chengxuan Lu*, Sanchen Xu, Peikun Wang, Xuefei Li, Haijun Ma, Hua Tong, Xinyi Zhou and Jiamin Zhao

School of Materials Science and Engineering, Shandong Jianzhu University, Jinan 250101, China

* **Correspondence:** Email: A3426805749@126.com.

Abstract: To mitigate ionic transport through connected pores in anodic aluminum oxide (AAO), a multicomponent silica sol-gel sealing process was applied to AA6061. By varying concentrations of nano-silicon dioxide (SiO_2)—specifically, 0, 2, 4, and 8 $g \cdot L^{-1}$—the relationships among coating microstructure, electrochemical response, and corrosion resistance were systematically evaluated. The results indicate that the response to a SiO_2 concentration of 2 $g \cdot L^{-1}$ is the most favorable among the tested concentrations. The number of open pores decreased, pore apertures narrowed, and cross-sectional densification was enhanced by this concentration. The total resistance, contributed by both porous and barrier layers, was 191 $k\Omega \cdot cm^2$. The corrosion current density decreased to 0.61 $\mu A \cdot cm^{-2}$. The sealed coating showed a lower corrosion rate in phosphoric acid immersion and maintained surface integrity after 720 h of neutral salt spray exposure. These findings indicate that silica is incorporated within the pores, effectively filling and extending diffusion pathways. As a result, the pores become less accessible, and the connectivity of the pore network is reduced. The results indicate an effective range of SiO_2 concentration for anodized AA6061, where improved corrosion resistance and enhanced protective characteristics of the anodic oxide layer contribute to greater material durability in corrosive environments.

Keywords: AA6061; AAO; sol-gel; corrosion resistance; nano-silicon dioxide

1. Introduction

AA6061, a heat-treatable Al-Mg-Si alloy, is widely used in aerospace structures, transportation equipment, and related industrial applications due to its favorable combination of strength, formability, and age hardening capability [1–3]. It is also commonly employed in marine structures, automotive components, and other applications requiring corrosion-resistant lightweight materials. However, exposure to environments containing chloride ions and high humidity can promote localized corrosion. As a result, surface engineering is necessary to stabilize the passive oxide layer, and surface modification is critical for achieving durability. Anodic aluminum oxide (AAO) enhances corrosion and wear resistance through the formation of a dense, adherent oxide layer on the substrate under an applied electric field [4–7]. The AAO microstructure comprises a compact barrier layer and a porous outer layer. The porous channels facilitate ionic transport, which necessitates sealing as a critical treatment to ensure stability [8,9]. Thus, enhancing sealing quality and interfacial bonding contributes to extended service life, reduced energy consumption, and lower environmental impact [10].

A wide range of sealing technologies has been developed in industry and academia [11–13]. Conventional hot water sealing relies on boehmite (AlOOH), which causes volumetric swelling and pore aperture constriction [6]. This method is simple and scalable; however, it requires high temperatures, which can cause pore shrinkage and microcracks, lowering low-frequency impedance and coating durability, thereby reducing the low-frequency impedance and compromising the coating's durability [14,15]. In response to sustainability goals, room temperature sealing methods have been developed, such as nickel salt processes and organic and inorganic hybrids, which can reduce energy consumption while maintaining or improving barrier properties [16,17]. Among these, sol-gel silanization with silane precursors or nano-SiO_2 can simultaneously achieve pore densification and interfacial stabilization, making it an effective AAO sealing approach that combines pore filling with interface bonding [14,18–22]. Recent studies have further advanced catecholamine and dopamine-assisted sol-gel strategies, demonstrating enhanced barrier properties and long-lasting corrosion protection on light alloys [23,24].

Single-component sealing systems include traditional hydrothermal methods as well as various chemical sealants [3]. Among them, nickel salt sealing has been widely applied due to its simplicity and high processing efficiency [4]. However, environmental concerns regarding nickel effluents promote searching for alternative, nickel-free sealing processes. In this context, rare-earth salt sealing provides a chromium-free, environmentally benign solution with comparable performance [19]. Previous studies reported that sealing anodic oxide coatings with cerium salts at 25 or 65 °C yields corrosion resistance comparable to hot water sealing, highlighting the role of inhibitor deposition and active redox species in stabilizing the interface [10,25]. Multicomponent sealants utilize the synergistic action of inorganic and organic components. The addition of polymers improves pore filling and mechanical toughness, reduces shrinkage stresses, and enhances resilience under thermal mechanical cycling [26–28].

Inorganic sealants, such as nano-SiO_2 sols, derive their effectiveness from their fine particle size, which enables deep pore penetration and uniform coverage of pore walls. It has been shown that nano-SiO_2 can infiltrate and fill nanochannels in a process that may include anodization followed by reimpregnation with SiO_2 sol, creating internal networks responsible for enhancing the density of films [3]. From a transport perspective, these networks reduce effective porosity, increase diffusion tortuosity, and restrict accessible ion pathways, while siloxane bonding enhances the local dielectric

properties of the barrier layer [26,29,30]. However, the sealing efficacy exhibits a strong dependence on concentration. At a moderate nano-SiO_2 concentration, well-dispersed nanoparticles are capable of penetrating into AAO nanochannels and facilitating in-pore condensation to form a continuous siloxane network, thereby reducing electrolyte uptake and increasing the tortuosity of ionic transport pathways [31,32].

In general, it is observed that sol-gel sealing enhances corrosion resistance but concurrently introduces some problems, such as brittleness caused by silica-rich regions or defects created by drying shrinkage. For this purpose, some researchers added various additives, such as graphene oxide, or applied hybrid modifications to improve crack resistance, interfacial adhesion, and overall coating performance. Sealing approaches have evolved from single-component organic or inorganic systems to multicomponent hybrid formulations. Among them, nano-SiO_2 sols are considered one of the most promising environmentally compatible and effective options, as they combine physical occlusion of pores with chemical bonding at moderate temperatures, compatible with scalable production [12,33–36]. Silica-based sealing is attractive because nano-SiO_2 can penetrate and occlude AAO pores, form an Si-network that strengthens the dielectric/barrier response, and provide a nickel/chromium-free route compatible with low-temperature, scalable processing [1,31,37]. Despite these benefits, the optimal concentration range for nano-SiO_2 sealants remains insufficiently defined. Concentration-dependent variations in microstructure and interfacial chemistry, including sol viscosity, particle interactions, gelation kinetics, and the evolution of silanol and siloxane species, require systematic evaluation under controlled chemical conditions and consistent film thickness [38]. Similarly, obtaining a sealing performance comparable to that of the high-temperature hydration treatment without losing mechanical integrity remains a significant technical challenge [39,40]. Determining the optimal SiO_2 concentration that maximizes the continuity of the barrier layer, while preventing surface enrichment and microcrack formation, is critical for establishing reliable correlations between pore filling efficiency and the electrochemical impedance responses of both porous and barrier layers [28].

To address these issues, nano-SiO_2 was incorporated into a silica-based sol-gel sealing system, and a multiscale measurement was used to investigate how concentration governs microstructure and performance. A series of SiO_2 concentration levels was applied to anodized AA6061 specimens for evaluating their influence on the AAO morphology and corrosion resistance. The pore transport behavior and the interfacial electrochemical reactions were analyzed. This study systematically evaluates how SiO_2 concentration governs silica deposition within pores and the resulting interfacial transport properties.

2. Materials and methods

2.1. Materials and reagents

The substrate employed in this study was 6061 aluminum alloy sheets with dimensions of 77 × 83 × 1.5 mm. The chemicals used included polyethylene glycol (PEG) (analytical grade, Tianjin Fuyu Fine Chemical Co., Ltd., Tianjin, China), anhydrous ethanol (EtOH) (analytical grade, Shandong Ke yuan Biochemical Co., Ltd., Shandong, China), cetyltrimethylammonium bromide (CTAB) (analytical grade, Shandong Ke yuan Biochemical Co., Ltd., Shandong, China), silane coupling agent (APTES) (analytical grade, Tianjin Fuyu Fine Chemical Co., Ltd., Tianjin, China), tetraethyl orthosilicate (TEOS) (analytical grade, Shanghai Leyan Medical Technology Co.,

Ltd., Shanghai, China), tetrapropylammonium hydroxide (TPAOH) (analytical grade, Shanghai Maclean Biochemical Technology Co., Ltd., Shanghai, China), nitric acid (HNO_3) (analytical grade, Qingdao, China), sodium hydroxide (NaOH) (analytical grade, Tianjin Hengxing Chemical reagent Manufacturing Co., Ltd., Tianjin, China) and deionized water.

2.2. Anodic oxidation and sealing preparation process and parameters

Specimens underwent degreasing, alkaline etching, nitric acid brightening, sulfuric acid anodizing, and subsequent sealing. The pretreatment stage involved alkaline etching and degreasing in NaOH (50 $g \cdot L^{-1}$) at room temperature for 2 min, followed by rinsing with deionized water. Subsequently, the samples were immersed in HNO_3 (ρ = 1.42 $g \cdot mL^{-1}$, 400 $g \cdot L^{-1}$) for brightening treatment until a uniform surface appearance was achieved, then rinsed again with deionized water and air-dried. Full parameter values are listed in Table 1. Anodizing was carried out in a sulfuric acid electrolyte (H_2SO_4) with a pH of 0.2–0.8, measured at 25 °C. The electrolyte contained 150–200 $g \cdot L^{-1}$ H_2SO_4, and the dissolved Al^{3+} concentration was maintained below 20 $g \cdot L^{-1}$ throughout anodizing. AA6061 samples were used as anodes and lead plates as cathodes, maintaining an anode-to-cathode area ratio of approximately 1:10. A constant voltage of 18 ± 0.4 V was applied using a regulated power supply (*KGF100V24A*, Zhejiang Yuanhong), resulting in a current density of 1.0 ± 0.2 $A \cdot dm^{-2}$. During this anodic oxidation, aluminum at the anode is oxidized to form an aluminum oxide layer (Al_2O_3). The porous structure of the anodic aluminum oxide is formed due to the competition between field-assisted oxide growth at the metal/oxide interface and simultaneous chemical dissolution of the oxide in the acidic electrolyte, resulting in a compact barrier layer beneath a porous outer layer. Under the applied electric field, Al^{3+} migrates outward while O^{2-}/OH^- migrates inward, and the balance between oxide formation and dissolution governs pore development and film morphology. The electrolyte was mechanically stirred and kept at a temperature of 20 ± 2 °C for a duration of 30 min. Following anodization, the specimens were rinsed with deionized water.

Table 1. Anodizing and sealing process parameters.

Anodizing conditions	Parameters	Sealing conditions	Parameters
pH	0.2–0.8	Nano SiO_2 (nm)	15–25
Voltage (V)	18 ± 0.4	CTAB ($g \cdot L^{-1}$)	1.5–2.5
Current density ($A \cdot dm^{-2}$)	1 ± 0.2	PEG ($g \cdot L^{-1}$)	3–5
H_2SO_4 (ρ = 1.84 $g \cdot mL^{-1}$, $g \cdot L^{-1}$)	150–200	APTES ($g \cdot L^{-1}$)	7–9
Cathode material	Pb	TEOS ($g \cdot L^{-1}$)	302–342
Anode/cathode area ratio	1:10	TPAOH ($g \cdot L^{-1}$)	42–48
Anodizing time (min)	30	Sealing time (min)	20
Anodizing temperature (°C)	20 ± 2	Sealing temperature (°C)	25 ± 2

The nano-SiO_2 composite sol was prepared by dispersing SiO_2 nanoparticles in an ethanol–water mixture at a volume ratio of 3:1, followed by the sequential addition of PEG, CTAB, and APTES under continuous stirring at ambient temperature to yield modified SiO_2. In a separate procedure, TEOS was hydrolyzed at 40 °C using TPAOH as the catalyst. The modified SiO_2 dispersion was subsequently introduced into the sol under mechanical stirring. Then, the mixture was heated to 40 °C

and stirred until a homogeneous sol was achieved. For sol-gel sealing, the samples were immersed in the low-viscosity silica sol at 25 ± 2 °C for 20 min, gently rinsed with deionized water, and isothermally cured at 25 ± 2 °C to facilitate complete gelation and drying. For hot water sealing, anodized samples were immersed in deionized water at 98 ± 2 °C for 20 min. A total of six sample groups were prepared: unsealed, hot water sealed, and sol–gel sealed samples with SiO_2 concentrations of 0, 2, 4, and 8 $g \cdot L^{-1}$, where the 0 $g \cdot L^{-1}$ condition refers to base sol without nano-SiO_2 nanoparticles.

2.3. Sample characterization

2.3.1. Micromorphology and chemical structure analysis

The surface and cross-sectional microstructures of the prepared samples under an acceleration voltage of 5–10 kV were observed using a Zeiss UltraTM55 scanning electron microscope (SEM) (Carl Zeiss, Oberkochen, Germany) and a secondary electron signal. The chemical composition of the coating was analyzed using energy-dispersive spectroscopy (EDS) based on SEM, and the EDS results were semiquantitative. The surface chemical structure of the prepared samples was examined using a Bruker VERTEX 70 Fourier-transform infrared spectrometer (FTIR) (Bruker Optik GmbH, Ettlingen, Germany), operating in attenuated total reflection mode; spectra were collected in the range 400–1200 cm^{-1}.

2.3.2. Electrochemical tests

All electrochemical tests were conducted on a CHI760E electrochemical workstation (Shanghai Chenhua Instrument Co., Ltd., Shanghai, China) in 3.5 wt.% NaCl at 25 ± 2 °C using a three-electrode configuration with a saturated calomel reference electrode, a platinum counter electrode, and the sample as the working electrode. The geometrically exposed working area was fixed at 1 cm^2 using a chemically resistant mask with a square aperture. After the open circuit potential stabilized, measurements were carried out sequentially. First, electrochemical impedance spectroscopy (EIS) was performed from 10^5 to 10^{-1} Hz; next, a Tafel polarization scan was conducted with an applied window of ± 300 mV around the Open-Circuit Potential (OCP) at 1 $mV \cdot s^{-1}$ to obtain corrosion current density (i_{corr}) and corrosion potential (E_{corr}). For each condition, measurements were conducted on at least three independent specimens. The corrosion rate (v_{corr}) was calculated from the polarization-derived i_{corr} according to ASTM G102 [41]: $v_{corr} = 0.00327 \times i_{corr} \times EW/\rho$, where i_{corr} is in $\mu A \cdot cm^{-2}$, EW is the equivalent weight of aluminum (8.99 $g \cdot equiv^{-1}$), and ρ is the density of aluminum (2.70 $g \cdot cm^{-3}$). All potentials are reported versus the saturated calomel electrode (SCE) and are denoted as V_{SCE}.

2.3.3. Corrosion performance tests

Short-term chemical resistance was evaluated following GB/T 8753.1-2017 with an exposed specimen area of 0.154 dm^2. Each sample was immersed in a phosphoric acid solution at 38 ± 2 °C for 13 min, then removed, rinsed with deionized water, dried to a constant weight, and weighed [42]. The mass loss rate (δ) was calculated from the mass loss per unit area and per minute ($mg \cdot dm^{-2} \cdot min^{-1}$). Each condition was assessed using no fewer than three specimens. All quantitative results are reported as mean ± standard deviation (SD) based on three independent specimens (n = 3). Long-term corrosion

resistance was evaluated by ASTM B117 neutral salt spray [43]. The evaluation index was the number of surface pits at 336 h, assessed over a 0.525 dm^2 central window [44]. The appearance of the samples was also recorded after 720 h.

3. Results and discussion

3.1. Microscopic morphology

Surface SEM images illustrate the pore architecture and surface texture that influence electrolyte penetration. The images show variations in pore diameter and aperture size, with some open pores disappearing. Microcrack initiation along pore walls is also observed, reflecting the effects of the sealing treatment [45]. These smaller pore apertures and reduced microcracking reflect higher tortuosity of the diffusion paths and a reduction of low resistance pathways for electrolyte ingress [35]. These modifications reduce electrolyte intrusion and thus help stabilize interfacial reactions during corrosion exposure.

As shown in Figure 1, the surface morphology of the AAO coating systematically varies with the nano-SiO_2 sealing concentration. For the sample without SiO_2 nanoparticle sealing, the surface exhibits the typical honeycomb porous AAO structure, although partial pore coverage by the sol-gel is apparent (Figure 1a,b). Pore openings remain abundant but appear moderately constricted in certain regions. The surface topography exhibits gentle undulations rather than marked step features. Fine microcracks appear sporadically and do not form a continuous network. In general, access to the porous layer by the electrolyte is still possible. Incipient gel formation within the pores reduces the effective aperture of some channels, indicating that only limited pore filling has occurred at this stage rather than complete sealing. As reported in [45], pore sealing results in a smoother outer surface and a reduction in pore opening size in anodized alumina, which aligns with the current observations.

When the concentration increases to 2 $g \cdot L^{-1}$ SiO_2, the visible surface pores significantly decrease, leading to a smoother and more planar surface topography. As shown in Figure 1c,d, fine silica particles are uniformly distributed across the surface. These characteristics are consistent with physical pore blockage and constriction near pore entrances. Thus, the effective number of apertures decreases while the distribution of apertures becomes narrower. Deposited particles remain discrete and homogeneously dispersed, maintaining uniform surface morphology. Moreover, sharp notches at the junction of ridges are less pronounced, which suggests fewer sites potentially inducing crack initiation [5]. Generally, infilling inside the surface region contributes to the improvement in structural stability in the outer porous layer and restricts further crack propagation. Such pore-mouth constriction together with more uniform in-pore silica deposition is expected to reduce the connectivity of transport channels, suppress electrolyte uptake, and delay chloride access to the barrier layer, thereby improving corrosion resistance relative to the unsealed states [31,32,37].

By contrast, with higher SiO_2 concentrations, as shown in Figure 1e–h, a silica-rich surface region is formed, characterized by particles aggregating into nodules and agglomerates [1]. The topography of the surface becomes much more irregular, though some residual channels can still be seen from the incomplete filling. Higher viscosity and greater interactions among the particles in those solutions promote early gelation and agglomeration near the pore entrances, restricting deeper infiltration. A similar trend of reduced pore penetration and preferential surface enrichment under less favorable sol conditions has been reported in the sol-gel sealing of porous anodic layers, where such effects

inherently constrain the extent of achievable barrier enhancement [31,37]. As a result, poor penetration of sol-gel and incomplete filling of deeper pores lead to a non-uniform sealing coverage with some structural defects, which may weaken its corrosion resistance.

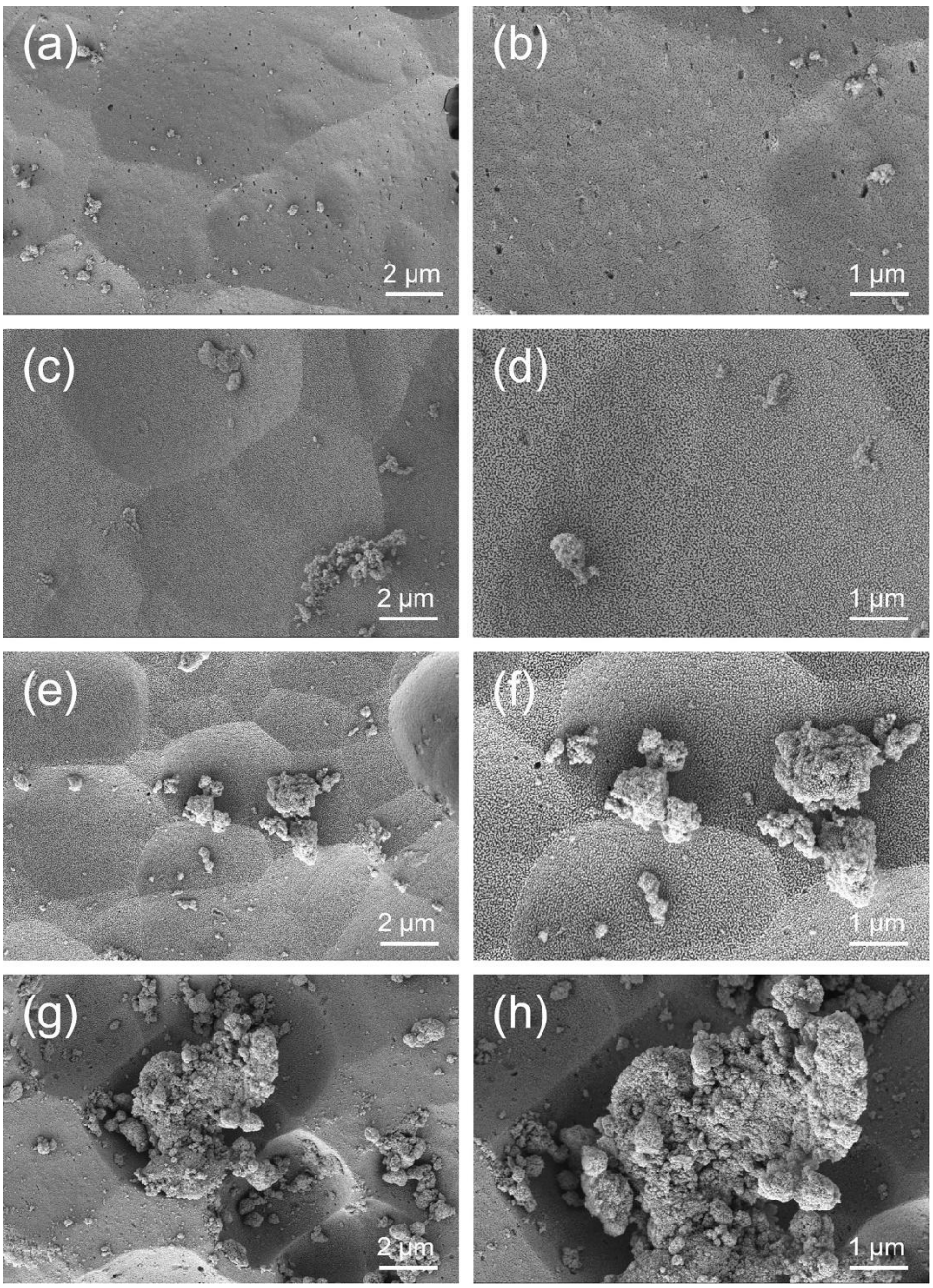

Figure 1. SEM micrographs of the AAO coating surface with different nano-SiO_2 contents at various magnifications. (a, b) No SiO_2; (c, d) 2 $g \cdot L^{-1}$; (e, f) 4 $g \cdot L^{-1}$; (g, h) 8 $g \cdot L^{-1}$. (a, c, e, g): 5,000×; (b, d, f, h): 10,000×.

Cross-sectional SEM was used to further investigate the sealing performance and structural continuity of the oxide layer. It is apparent from the cross-sectional images in Figure 2a,b that there is no difference in the morphology of the 2 $g \cdot L^{-1}$ SiO_2-treated sample for multiple fields of view. The

coating-substrate interface is mainly linear and continuous, with only slight undulations. Specifically, no visible cracks, localized delamination, or internal defects are detected. These observations imply that a dense, continuous oxide coating with extended diffusion paths was formed [46,47]. Such a structure is associated with reduced crack propagation and enhanced barrier effectiveness [48].

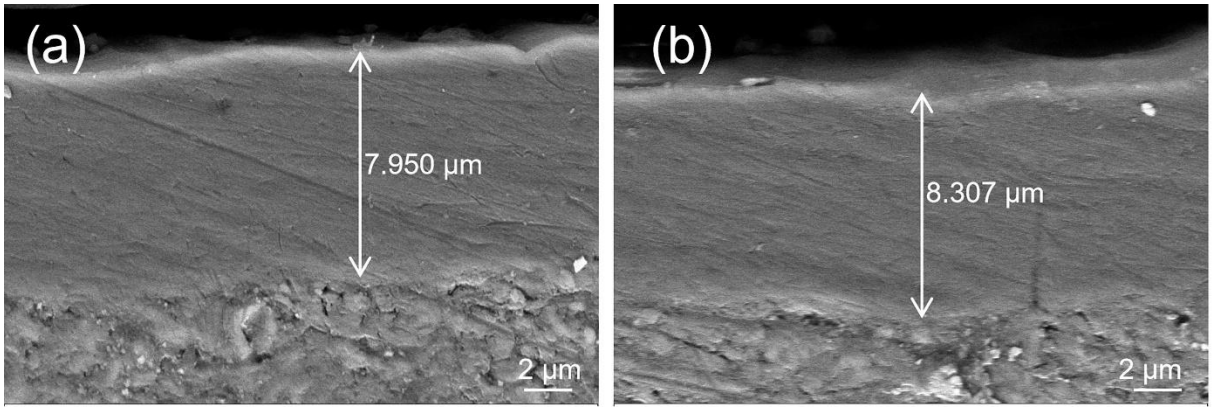

Figure 2. Cross-sectional SEM of the 2 $g \cdot L^{-1}$ SiO_2 sealed sample. (a, b): 10,000×.

According to SEM analysis, orderly changes in the pore geometry and surface ridges are depicted for different conditions of sealing. Open apertures at 2 $g \cdot L^{-1}$ are less frequent, and the contours at the junctions between ridges are smooth. This corresponds to the better structural integrity of the outer porous layer observed in the studied regions. Such morphological changes decrease the number of possible pathways that electrolytes can easily take to penetrate the oxide coating. It also leads to an increase in tortuosity of surface diffusion paths, which denotes lower permeability through accessible channels and reflects enhanced barrier performance. The present results give a morphological basis to subsequent EDS and FTIR characterization of spatial silica distribution.

3.2. Elemental distribution and chemical structure analysis

Elemental distribution maps of Si, O, and Al are shown to evaluate the uniformity of the silica sealing agent distribution within the porous oxide network. As shown in Figure 3, the elemental distribution maps reveal that the spatial distributions of Si and O vary under each sealing condition. In the sample without SiO_2 nanoparticle sealing, only minimal Si signals are detected in the surface EDS analysis, as shown in Figure 3a–c, appearing as isolated spots or short streaks.

For the sample sealed with 2 $g \cdot L^{-1}$ SiO_2, elemental maps (Figure 3d–f) of silicon and oxygen present consistently high intensities and a uniform distribution. Semiquantitative EDS shows a content of about 4.7 wt.% of silicon with a corresponding marginal decrease in aluminum. The continuous Si signal throughout the pore walls and around apertures displays a small spatial variation and no obvious low-intensity zone. This means SiO_2 is uniformly incorporated into the pore structure, homogeneously distributing across the pore surfaces and on the outer layer, enhancing its homogeneity and densification [49,50]. With increased SiO_2 concentration to 4 and 8 $g \cdot L^{-1}$, there is a gradual increase in the overall silicon content on the surface. However, a big difference in its spatial distribution was disclosed. In Figure 3g–l, strong Si signals are shown at the surface and within clustered colloidal regions, evidencing preferential silica accumulation at the outer layer and restricted inward diffusion.

This is associated with reduced compositional uniformity and discontinuous sealing across the coating thickness.

The FTIR spectrum of the sol-gel sealed AAO coating presents characteristic absorption peaks associated with Si–O–Si bonds, indicating the incorporation of nano-SiO_2 into the coating structure [1]. These peaks are indications of the formation of a silica network within the pores of the AAO surface [51,52]. The identification of these functional groups supports the characterization of the structural features of the sealing layer.

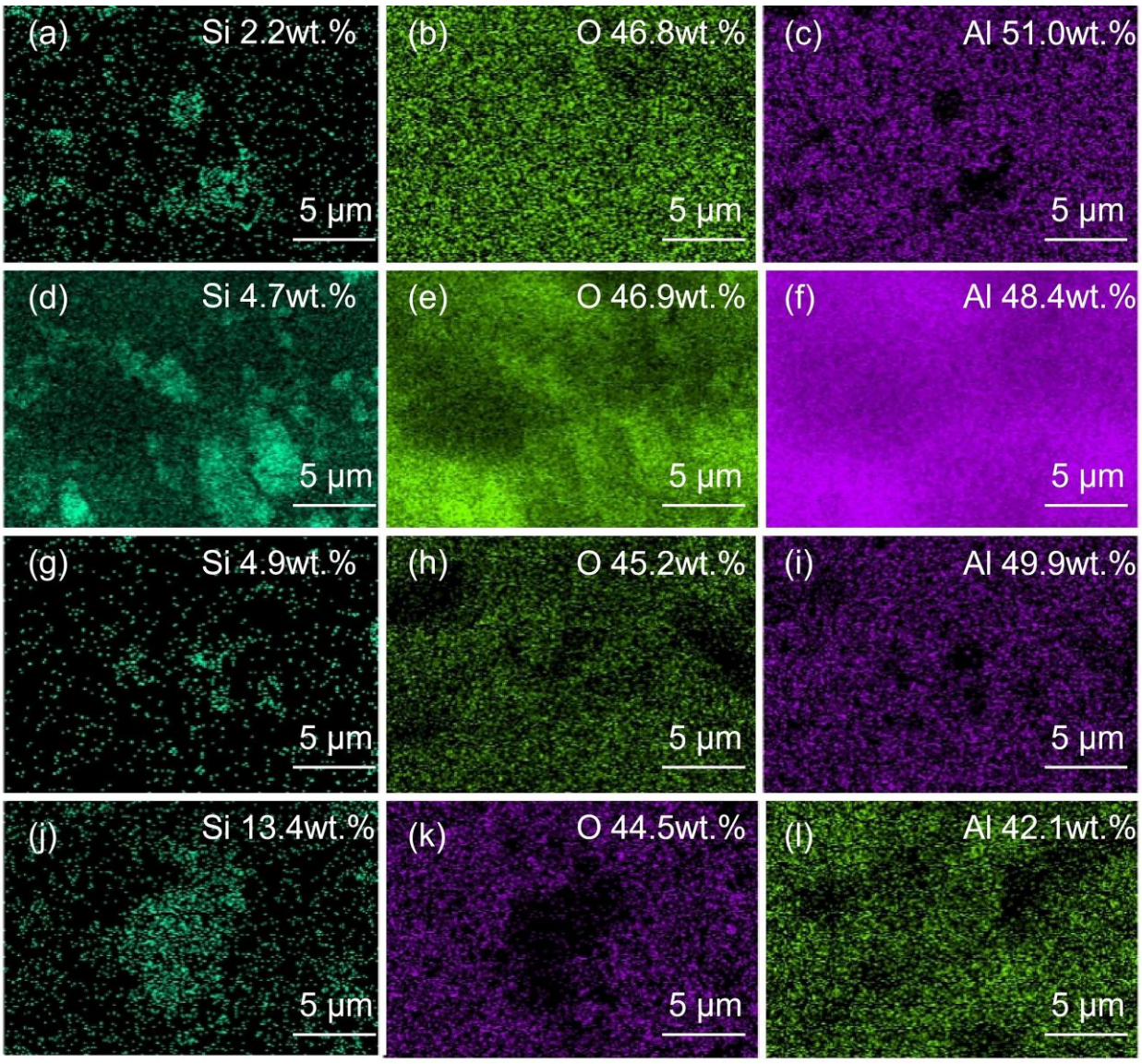

Figure 3. Elemental distribution maps. (a, b, c) No SiO_2; (d, e, f) 2 $g \cdot L^{-1}$ SiO_2; (g, h, i) 4 $g \cdot L^{-1}$ SiO_2; (j, k, l) 8 $g \cdot L^{-1}$ SiO_2.

As shown in Figure 4, the strong absorption bands at 1081 and 1042 cm^{-1} were ascribed to asymmetric stretching vibrations of the Si–O–Si bonds in an amorphous siloxane network. The splitting of the main band, accompanied by a distinct shoulder, evidenced network linking and short-range structural disorder typical of sol–gel-derived silica. A low-frequency band observed at about 445 cm^{-1} corresponded to Si–O–Si bending vibrations and furnished additional spectroscopic

evidence for the presence of the siloxane framework [51–54]. On the whole, the typical Si–O–Si stretching and bending vibrations pointed to amorphous silica formation via pore condensation, although the possible densification in the sealed layer could contribute to a decrease in the pore connectivity.

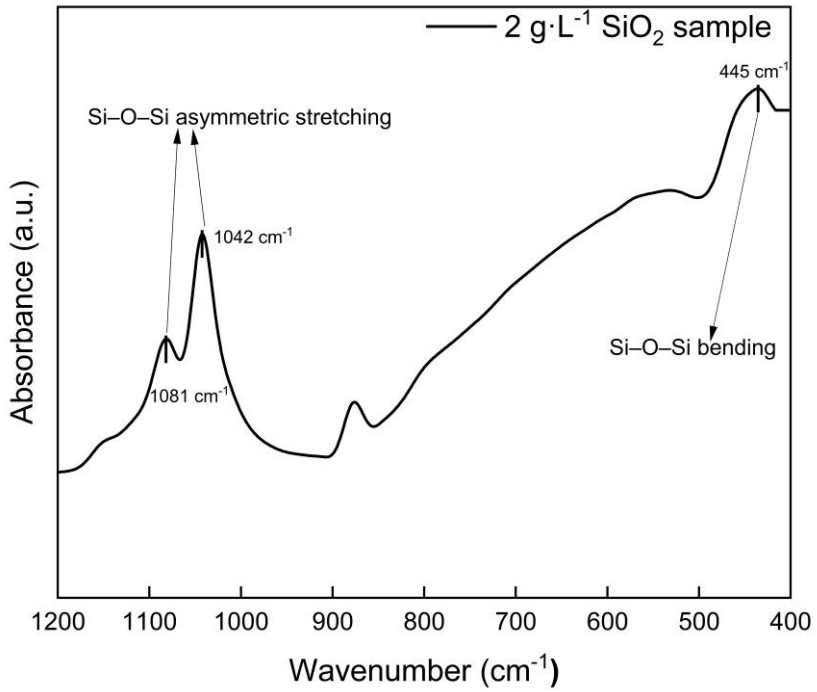

Figure 4. Fourier transform infrared (ATR) spectrum of the nano-SiO_2 sealed sample.

The combined EDS and FTIR analyses indicate that nano-SiO_2 undergoes condensation within the pores to form an interconnected network and thereby may develop a continuous Si–O–Si framework throughout the porous layer [54]. When the SiO_2 concentration is 2 $g \cdot L^{-1}$, uniformly distributed silica reduces compositional discontinuities, which is related to the increased densification of the barrier layer with fewer defects. Such a transformation from discrete silica deposits into a continuous amorphous siloxane network is coherent with the sealing mechanism shown above from the SEM images. These findings provide chemical evidence for enhanced coating compactness and establish a fundamental basis for interpreting the electrochemical impedance and Tafel polarization behavior of the sealed coatings.

3.3. Electrochemical corrosion performance

The EIS responses were interpreted using a two-time-constant model representing porous and barrier layers [54]. The Nyquist plot (Figure 5a), fitted with two-time-constant model (Figure 5b), shows a single depressed semicircle with a high-frequency shoulder. In contrast, the Bode magnitude (Figure 5c,d) exhibits a low-frequency rise in |Z|. In the Bode phase plot (Figure 5d), two distinct peaks are observed: one at high frequency, corresponding to the porous layer [55,56], and another in the mid to low frequency range, associated with the barrier layer [56,57], indicating the presence of two time constants. These features are reproduced by the two-time-constant equivalent circuit in Figure 5b, representing the porous outer layer and the barrier inner layer, respectively. Constant phase elements (Q and n) account for non-ideal capacitive behavior arising from interfacial

heterogeneity ($0 < n \leq 1$, with n approaching 1 indicating a response closer to an ideal capacitor); in the equivalent-circuit fitting, n_p and n_b are the *CPE* exponents for the porous-layer and barrier-layer responses, respectively, and the reduced dispersion after sealing is reflected by n values closer to unity, indicating a more homogeneous dielectric/interface [58]. A decrease in Q dispersion has similarly been associated with reduced interfacial heterogeneity in anodized films [59]. Although two arcs are not evident on the Nyquist plot, a phase response with two peaks indicates a two-time-constant behavior attributable to the porous and barrier layers [36].

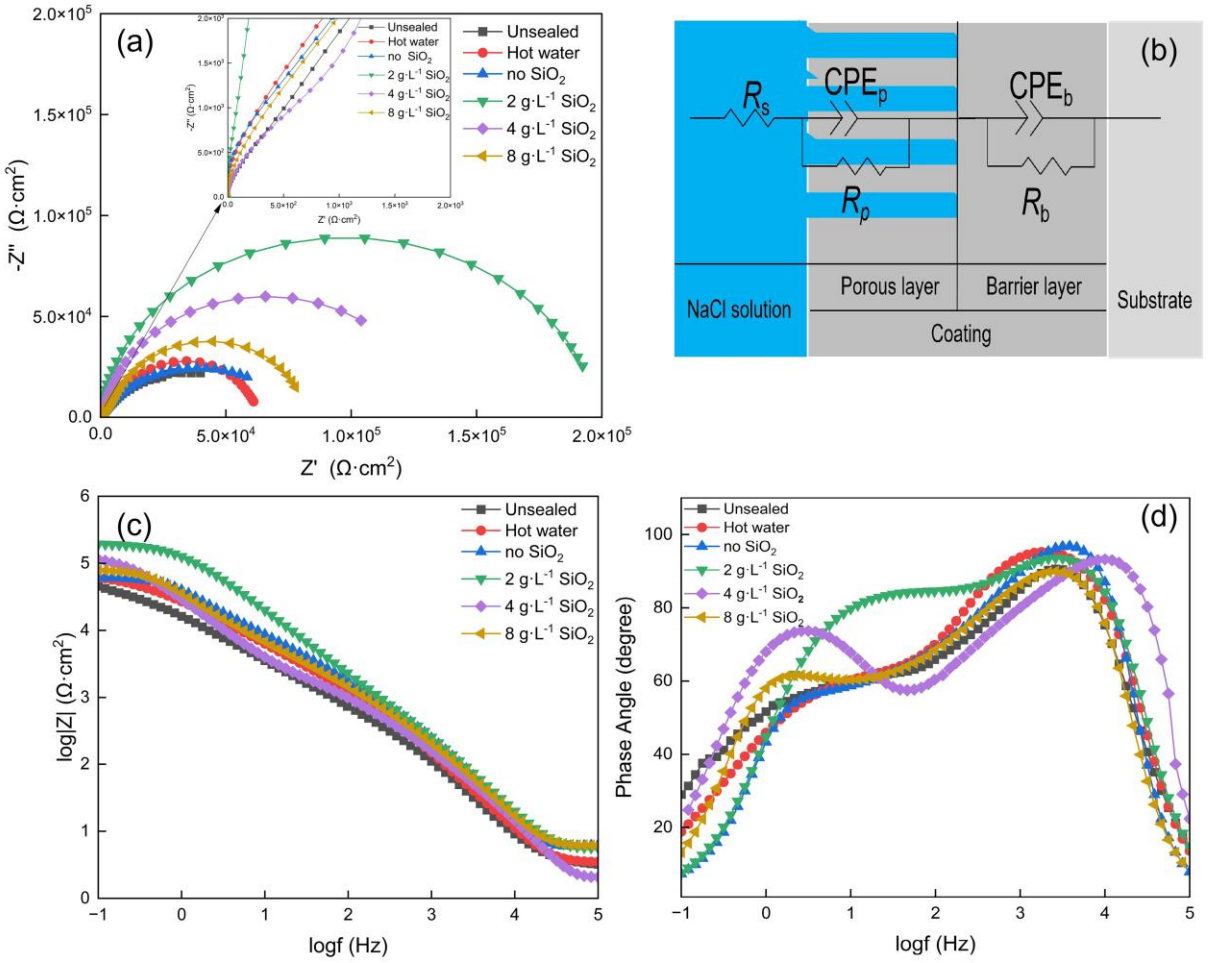

Figure 5. EIS spectra and equivalent circuits: (a) Nyquist plot; (b) equivalent circuit; (c) Bode magnitude plot; and (d) Bode phase plot.

For the unsealed, hot water, no SiO_2, and 2, 4, and 8 $g \cdot L^{-1}$ SiO_2 samples, the Nyquist plots exhibit small, flattened, high-frequency arcs with steep low-frequency tails. Correspondingly, the Bode plots show lower and less stable low-frequency impedance plateaus and narrower phase angle plateaus. In contrast, the 4 and, especially, the 8 $g \cdot L^{-1}$ SiO_2 treatments yield more depressed arcs with overall lower low-frequency |Z|, indicating degraded protection and greater leakage of the corrosive medium through the porous layer.

At a SiO_2 concentration of 2 $g \cdot L^{-1}$, the impedance response exhibits the best corrosion resistance among all tested conditions. Improvements in both the porous and barrier layers are observed concurrently, suggesting a more effective sealing. By equivalent circuit modeling, as shown in Table 2,

it was obtained that the highest resistance of the porous layer (R_p) is about 95.1 kΩ·cm^2, and that of the highest barrier layer (R_b) is around 95.9 kΩ·cm^2. The porous layer is characterized by $Q_p = 0.10 \times 10^{-7}$ S·s^n·cm^{-2} and $n_p = 0.98$, while the barrier layer showed $Q_b = 10.0 \times 10^{-7}$ S·s^n·cm^{-2} and $n_b = 0.89$, which is indicative of an increase in effective dielectric thickness and reduced interfacial heterogeneity. Consistent interpretations have been reported for sol-gel sealed porous anodic layers, where a siloxane network decreases effective capacitance and elevates low-frequency impedance by limiting electrolyte transport through connected pores [60]. EIS responses further indicate the presence of a continuous amorphous silica network inside the pores of AAO with decreasing pore diameter and pore connectivity and increasing diffusion tortuosity. Correspondingly, the mid to low frequency peak would shift to the low frequencies, and the phase angle plateau would become broader, while |Z| values at 10^{-1} Hz would increase. Lower Q values reflect the more homogeneous distribution of the dielectric with fewer ionic conduction pathways, while the n values reflect the effective increase in dielectric spacing and densification of the porous structure [61]. Overall, the EIS characteristics show improved corrosion resistance compared to the unsealed or hot water–sealed samples.

Table 2. EIS fitting parameters.

Sample	R_p (kΩ·cm^2)	Q_P (10^{-7} S·s^n·cm^{-2})	n_p	R_b (kΩ·cm^2)	Q_b (10^{-7} S·s^n·cm^2)	n_b
Unsealed	0.861	230	0.74	44.4	219	0.79
Hot water	6.43	1.20	0.75	63.2	68.9	0.73
no SiO_2	7.93	0.11	0.79	54.2	28.5	0.75
2 g·L^{-1} SiO_2	95.1	0.10	0.98	95.9	10.0	0.89
4 g·L^{-1} SiO_2	65.9	0.12	0.77	75.1	38.7	0.85
8 g·L^{-1} SiO_2	4.45	7.19	0.75	82.5	66.4	0.77

To complement the EIS analysis, Tafel polarization curves were employed to further investigate the corrosion kinetics behavior of the sealed samples. Tafel curves reveal distinct electrochemical responses across the different sealing treatments (Figure 6).

Tafel analysis further indicates improved electrochemical behavior at 2 g·L^{-1} SiO_2. For comparison with the immersion tests, i_{corr} obtained from the polarization curves was further converted to the corrosion rate (v_{corr}) using the ASTM G102 relationship. According to Zheludkevich et al. [62,63], optimized sol-gel coatings on aluminum alloys typically exhibit corrosion current densities on the order of μA·cm^{-2}. As shown in Figure 6 and Table 3, the corrosion potential positively shifts to −0.548 V_{SCE}, while the corrosion current density decreases to 0.615 μA·cm^{-2}, corresponding to a corrosion rate of 0.0067 mm·a^{-1}. In comparison, the present system shows a lower i_{corr} and v_{corr}, indicating a further improvement in corrosion protection beyond conventional sol-gel-based coatings. Notably, compared with the unsealed sample, i_{corr} decreases about 26-fold with the sol sealing (no SiO_2) and 62-fold at 2 g·L^{-1}, evidencing effective silica–sol sealing and its further enhancement by nano-SiO_2. Within the tested range, the 2 g·L^{-1} SiO_2 sealing shows the lowest v_{corr} and therefore the slowest corrosion kinetics relative to the unsealed and hot water sealing, evidencing improved corrosion resistance. The decreased i_{corr} within a mixed potential view indicates slower interfacial kinetics at the E_{corr}. It is likely due to the partial blockage of the active sites for interfacial reactions by the silica gel, supported by decreased availability of pathways for reaction, thus leading to the inhibition of dissolution of aluminum and reduction of oxygen. These mutually reinforcing effects weaken aluminum dissolution

and oxygen reduction, shift the corrosion potential slightly positive, and lower the steady corrosion rate [64]. These Tafel inferences are consistent with the EIS results for the same condition.

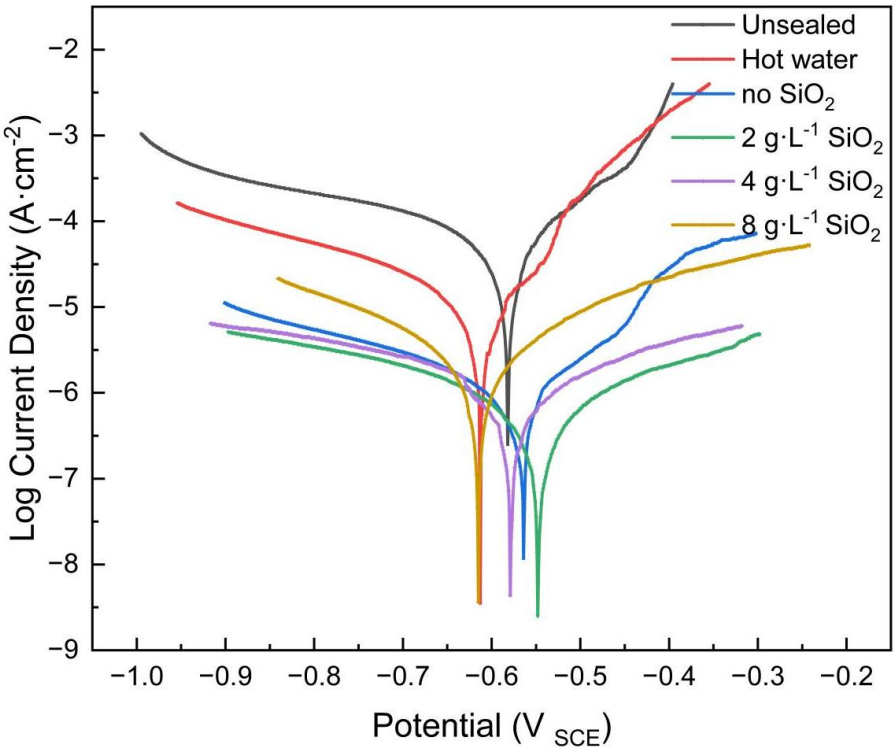

Figure 6. Tafel polarization.

Table 3. Tafel fitting parameters.

Sample	E_{corr} (V_{SCE})	i_{corr} ($\mu A \cdot cm^{-2}$)	v_{corr} ($mm \cdot a^{-1}$)
Unsealed	–0.582	38.2	0.416
Hot water	–0.615	8.39	0.0913
No SiO_2	–0.564	1.50	0.0163
2 $g \cdot L^{-1}$ SiO_2	–0.548	0.615	0.0067
4 $g \cdot L^{-1}$ SiO_2	–0.579	1.61	0.0175
8 $g \cdot L^{-1}$ SiO_2	–0.613	2.22	0.0242

Overall, the electrochemical responses indicate that nano-SiO_2 sol-gel sealing improves interfacial charge transfer resistance due to changes in the porous layer and barrier layer. Reduced connectivity of the pore restricts electrolyte access, whereas a more homogeneous distribution of dielectric material within the porous layer contributes to the stabilization of barrier layer polarization. These features are in agreement with improved interfacial passivation, where ion transport occurs along more tortuous, higher resistance pathways and is increasingly coupled to the barrier layer. The behavior exhibited is consistent with a sealing mechanism dominated by the growth of a silica network within the pores rather than by simple surface accumulation [28]. Subsequent corrosion tests were evaluated to determine whether these interfacial improvements remain under chemical dissolution and salt spray exposure, providing an assessment of the durability implications suggested by the electrochemical results.

3.4. Corrosion resistance assessment

Short-term phosphoric acid immersion mass loss rate testing measures the chemical durability of the sealed oxide layer against rapid dissolution, whereas neutral salt spray testing can also evaluate long-term corrosion resistance under continuous neutral salt spray exposure.

Figure 7 presents the mass loss rate results from phosphoric acid immersion testing. The coating sealed with 2 $g \cdot L^{-1}$ SiO_2 exhibits the lowest mass loss rate, $\delta \approx 1.2$ $mg \cdot dm^{-2} \cdot min^{-1}$, which is half that of the unsealed sample. This result is in accordance with an improved corrosion-resistant state achieved through sealing with 2 $g \cdot L^{-1}$ treatment. This macroscopic improvement is consistent with the polarization-derived corrosion rate (Table 3), where the 2 $g \cdot L^{-1}$ SiO_2 sample also exhibits the minimum v_{corr}. However, the further increase in the SiO_2 concentration to 4 and 8 $g \cdot L^{-1}$ leads to a higher mass loss rate, which reflects a concentration-dependent decrease in its short-term chemical stability. Accordingly, the higher mass loss rates at 4 and 8 $g \cdot L^{-1}$, consistent with their increased v_{corr} values, indicate that the polarization-derived corrosion kinetics are reflected in the immersion response.

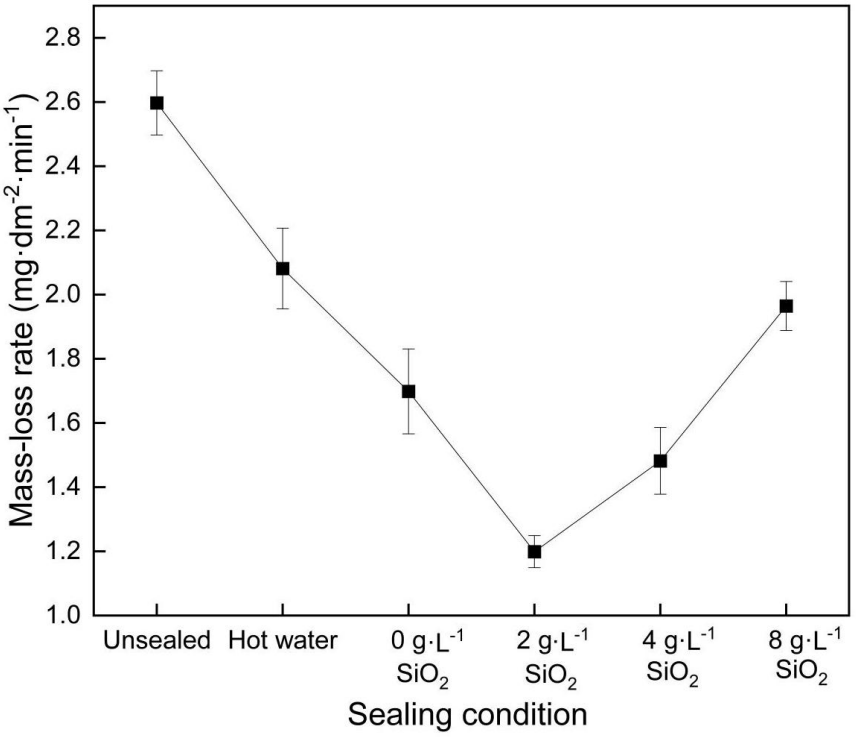

Figure 7. Mass loss in phosphoric acid immersion tests for samples sealed with various SiO_2 concentrations. Error bars: SD (n = 3).

Neutral salt spray testing further reveals differences in long-term durability among the sealed samples. Whereas after 336 h of exposure, the sample sealed with 2 $g \cdot L^{-1}$ SiO_2 did not present any visible pitting or white corrosion products, all other samples resulted in some forms of surface degradation. After 720 h of testing, the sample treated with 2 $g \cdot L^{-1}$ SiO_2 retained the integrity and continuity of the surface, hence suggesting resistance to prolonged corrosive conditions under the test protocol [65]. Comparable delays in pit initiation and enhanced Neutral Salt Spray (NSS) resistance following appropriate sealing have been documented for TSA (tartaric-sulfuric acid)-AA2024 systems [59].

Overall, the corrosion performance further corroborates the electrochemical interpretation. Limited electrolyte uptake and elongated diffusion paths are associated with suppressed localized dissolution and stabilized interfacial reactions, as reflected by higher resistive components and lower interfacial admittance. At the same time, mass loss rate and salt spray results also further demonstrate the increased impedance and reduced Q magnitudes observed in the impedance analysis of electrochemical behavior. All in all, the results of the immersion and salt spray tests back up the idea that, under the current conditions, sealing with 2 $g \cdot L^{-1}$ SiO_2 enhances the corrosion resistance of anodized AA6061. This translation of increased impedance into sustained macroscopic durability is consistent with previous EIS–NSS correlations, in which sol-gel filling was found to enhance pore resistance and extend exposure tolerance [66].

4. Conclusions

In this study, a silica-based nano-sealing process was systematically evaluated for AAO coatings formed on AA6061 alloy, with variation in nano-SiO_2 concentration. The results indicate that an optimal SiO_2 concentration significantly improves corrosion resistance. SEM and EDS analyses revealed fewer open apertures, smoother ridge junctions, and a more uniform silicon distribution after sealing with 2 $g \cdot L^{-1}$ SiO_2. These features, taken in conjunction with FTIR detection of Si–O–Si stretching and bending bands characteristic of an amorphous siloxane network, accord with silica immobilization at the pore throats and along internal walls, with densification of the surface. At higher SiO_2 concentrations, surface pores and microcracks appear, indicating deposition concentrated at the surface rather than within the pores. The enhanced corrosion resistance observed at a concentration of 2 $g \cdot L^{-1}$ can be attributed to an optimal balance between the formation of an intrapore network and the suppression of surface aggregation or premature gelation. This condition facilitates a significant reduction in pore connectivity while avoiding the development of defects associated with volumetric shrinkage.

Electrochemical measurements of the 2 $g \cdot L^{-1}$ SiO_2 sealed sample further exhibited higher impedance in both the porous and barrier layers. Such results, combined with the shift to nobler corrosion potential and lower corrosion rate, are in accordance with limited electrolyte penetration and more homogeneous dielectric response due to localized densification near the interface. The responses collectively indicate enhanced corrosion resistance across the tested range. Phosphoric acid immersion tests and neutral salt spray tests support this mechanism by indicating reduced material dissolution and better surface integrity at a concentration of 2 $g \cdot L^{-1}$. In contrast, higher SiO_2 concentrations result in sealing that is primarily concentrated at the surface, accompanied by microcrack formation, which facilitates ionic penetration and compromises durability. Overall, this study determined the feasible operating window that results in an enhancement of corrosion resistance that is both energy-efficient and scalable for sealing anodized AA6061.

Use of AI tools declaration

The authors declare they have not used Artificial Intelligence (AI) tools in the creation of this article.

Acknowledgments

This work was financially supported by the Natural Science Foundation of Shandong Province (ZR2024LLZ006) and the Key R&D Program of Shandong Province, China (Grant No. 2024TSGC0675 and No. 2025TSGCCZZB0007).

Author contributions

Chengxuan Lu: conceptualization, validation, formal analysis, investigation, resources, data curation, writing the original draft, writing—review & editing, supervision, project administration, funding acquisition; Sanchen Xu: methodology, validation, formal analysis, investigation, resources; Peikun Wang: software, formal analysis, investigation, data curation, visualization (Figures), supervision; Xuefei Li: validation, formal analysis, writing the original draft, project administration; Haijun Ma: formal analysis, resources, data curation, funding acquisition; Hua Tong: methodology, software, visualization (Figures); Xinyi Zhou: conceptualization, funding acquisition; Jiamin Zhao: methodology, visualization (Figures), supervision.

Conflict of interest

All authors declare no conflicts of interest in this paper.

References

1. Ofoegbu SU, Fernandes FAO, Pereira AB (2020) The sealing step in aluminum anodizing: A focus on sustainable strategies for enhancing both energy efficiency and corrosion resistance. *Coatings* 10: 226. https://doi.org/10.3390/coatings10030226
2. Razzouk E, Koncz-Horváth D, Török TI (2024) Critical challenges in the anodizing process of aluminium–silicon cast alloys—A review. *Crystals* 14: 617. https://doi.org/10.3390/cryst14070617
3. Paz Martínez-Viademonte M, Abrahami ST, Hack T, et al. (2020) A review on anodizing of aerospace aluminum alloys for corrosion protection. *Coatings* 10: 1106. https://doi.org/10.3390/coatings10111106
4. Jo H, Lee S, Kim D, et al. (2020) Low temperature sealing of anodized aluminum alloy for enhancing corrosion resistance. *Materials* 13: 4904. https://doi.org/10.3390/ma13214904
5. Ono S (2021) Nanostructure analysis of anodic films formed on aluminum-focusing on the effects of electric field strength and electrolyte anions. *Molecules* 26: 7270. https://doi.org/10.3390/molecules26237270
6. Ono S, Asoh H (2021) Mechanism of hot water sealing of anodic films formed on aluminum. *Corros Sci* 181: 109221. https://doi.org/10.1016/j.corsci.2020.109221
7. Capelossi VR, Poelman M, Recloux I, et al. (2014) Corrosion protection of clad 2024 aluminum alloy anodized in tartaric-sulfuric acid bath and protected with hybrid sol-gel coating. *Electrochim Acta* 124: 69–79. https://doi.org/10.1016/j.electacta.2013.09.004

8. Agustín-Sáenz C, Martín-Ugarte E, Pérez-Allende B, et al. (2021) Effect of ethylene glycol dimethacrylate on VOC reduction, rheological, mechanical and anticorrosion properties of a hybrid sol-gel coating on AA2024-T3 and sulfuric acid anodized AA2024-T3. *Prog Org Coat* 159: 106408. https://doi.org/10.1016/j.porgcoat.2021.106408
9. Collazo A, Ezpeleta I, Figueroa R, et al. (2020) Corrosion protection properties of anodized AA2024T3 alloy sealing with organic-based species. *Prog Org Coat* 147: 105779. https://doi.org/10.1016/j.porgcoat.2020.105779
10. Covelo A, Rodil S, Nóvoa XR, et al. (2022) Development and characterization of sealed anodizing as a corrosion protection for AA2024-T3 in saline media. *Mater Today Commun* 31: 103468. https://doi.org/10.1016/j.mtcomm.2022.103468
11. Scampone G, Timelli G (2023) The influence of sealing processes and machining operations on the scratch and wear resistance of anodized AlSi9Cu3(Fe) diecasting alloy. *JOM* 76: 196–208. https://doi.org/10.1007/s11837-023-06241-3
12. Yasakau KA, Kuznetsova A, Kallip S, et al. (2018) A novel bilayer system comprising LDH conversion layer and sol-gel coating for active corrosion protection of AA2024. *Corros Sci* 143: 299–313. https://doi.org/10.1016/j.corsci.2018.08.039
13. Druart ME, Recloux I, Thai TT, et al. (2016) Impact of the addition of cerium salts (Ce(III) and Ce(IV)) on formation and ageing of a silica sol-gel layer. *Surf Coat Technol* 304: 40–50. https://doi.org/10.1016/j.surfcoat.2016.07.006
14. del Olmo R, López E, Matykina E, et al. (2023) Hybrid PEO/sol-gel coatings loaded with Ce for corrosion protection of AA2024-T3. *Prog Org Coat* 182: 107667. https://doi.org/10.1016/j.porgcoat.2023.107667
15. del Olmo R, Tiringer U, Milošev I, et al. (2021) Hybrid sol-gel coatings applied on anodized AA2024-T3 for active corrosion protection. *Surf Coat Technol* 419: 127251. https://doi.org/10.1016/j.surfcoat.2021.127251
16. Hou MY, Pan CC, Wang MY, et al. (2024) Improving the cavitation corrosion resistance of 6061 aluminum alloy by anodizing. *Electrochim Acta* 503: 144890. https://doi.org/10.1016/j.electacta.2024.144890
17. Yasakau KA, Starykevich M, Ferreira MGS, et al. (2021) A critical look at interpretation of electrochemical impedance spectra of sol-gel coated aluminium. *Electrochim Acta* 378: 138091. https://doi.org/10.1016/j.electacta.2021.138091
18. AlShamaileh E, Altwaiq AM, Esaifan M, et al. (2022) Study of the microstructure, corrosion and optical properties of anodized aluminum for solar heating applications. *Metals* 12: 1635. https://doi.org/10.3390/met12101635
19. Yu S, Wang L, Wu C, et al. (2020) Studies on the corrosion performance of an effective and novel sealing anodic oxide coating. *J Alloys Compd* 817: 153257. https://doi.org/10.1016/j.jallcom.2019.153257
20. Hao XL, Zhao N, Jin HH, et al. (2020) Nickel-free sealing technology for anodic oxidation film of aluminum alloy at room temperature. *Rare Met* 40: 968–974. https://doi.org/10.1007/s12598-020-01410-8
21. Li W, Liu P, Meng J, et al. (2016) Microstructure and mechanical property of TiSiN nanocomposite film with inserted CrAlN nanomultilayers. *Surf Coat Technol* 286: 313–318. https://doi.org/10.1016/j.surfcoat.2015.12.033

22. Wang YB, Huang QY, Zhou BT, et al. (2021) Corrosion protection of 6061 aluminum alloys by sol-gel coating modified with ZnLaAl-LDHs. *Coatings* 11: 478. https://doi.org/10.3390/coatings11040478
23. Li J, Wang LY, Bai HH, et al. (2023) Development of an eco-friendly waterborne polyurethane/catecholamine/sol-gel composite coating for achieving long-lasting corrosion protection on Mg alloy AZ31. *Prog Org Coat* 183: 107732. https://doi.org/10.1016/j.porgcoat.2023.107732
24. Li J, Li S, Chen C, et al. (2023) Dopamine self-polymerized sol-gel coating for corrosion protection of AZ31 Mg alloy. *Colloids Surf A* 666: 131283. https://doi.org/10.1016/j.colsurfa.2023.131283
25. Chen ZG, Zhang GF, Bobaru F (2015) The influence of passive film damage on pitting corrosion. *J Electrochem Soc* 163: C19–C24. https://doi.org/10.1149/2.0521602jes
26. Poznyak A, Pligovka A, Turavets U, et al. (2020) On-aluminum and barrier anodic oxide: Meeting the challenges of chemical dissolution rate in various acids and solutions. *Coatings* 10: 875. https://doi.org/10.3390/coatings10090875
27. Park J, Son K, Lee J, et al. (2021) Effects of anodizing conditions on thermal properties of Al 20XX alloys for aircraft. *Symmetry* 13: 433. https://doi.org/10.3390/sym13030433
28. Macera L, Pullini D, Boschetto A, et al. (2023) Sol-gel silica coatings for corrosion protection of aluminum parts manufactured by selective laser melting (SLM) technology. *Coatings* 13: 1081. https://doi.org/10.3390/coatings13061081
29. Lu BJ, Lin KT, Kuo YM, et al. (2021) Preparation of high-transparency, superhydrophilic visible photo-induced photocatalytic film via a rapid plasma-modification process. *Coatings* 11: 784. https://doi.org/10.3390/coatings11070784
30. Poznyak A, Pligovka A, Laryn T, et al. (2021) Porous alumina films fabricated by reduced temperature sulfuric acid anodizing: morphology, composition and volumetric growth. *Materials* 14: 767. https://doi.org/10.3390/ma14040767
31. Whelan M, Cassidy J, Duffy B (2013) Sol-gel sealing characteristics for corrosion resistance of anodised aluminium. *Surf Coat Technol* 235: 86–96. https://doi.org/10.1016/j.surfcoat.2013.07.018
32. Merino E, Durán A, Ceré S, et al. (2022) Hybrid epoxy-alkyl sol-gel coatings reinforced with SiO_2 nanoparticles for corrosion protection of anodized AZ31B Mg alloy. *Gels* 8: 242. https://doi.org/10.3390/gels8040242
33. Godja N, Munteanu FD (2025) Environmentally friendly solutions as potential alternatives to chromium-based anodization and chromate sealing for aeronautic applications. *Coatings* 15: 439. https://doi.org/10.3390/coatings15040439
34. Prada Ramirez OM, Kremmer TM, Marin JH, et al. (2023) Ce nanoparticles and sol-gel hybrid organic-inorganic coatings maximize corrosion protection in the anodized AA2024-T3. *Corros Sci* 221: 111330. https://doi.org/10.1016/j.corsci.2023.111330
35. Zandi Zand R, Verbeken K, Adriaens A (2012) Corrosion resistance performance of cerium doped silica sol-gel coatings on 304L stainless steel. *Prog Org Coat* 75: 463–473. https://doi.org/10.1016/j.porgcoat.2012.06.008

36. Adel M, Fathy DS, El-Eneen OA (2025) Environmentally sustainable epoxy nanocomposite coating reinforced with chitosan derived nitrogen doped graphene for enhanced corrosion resistance and mechanical performance. *Sci Rep* 15: 30617. https://doi.org/10.1038/s41598-025-11204-6
37. Fori B, Taberna PL, Arurault L, et al. (2012) Electrophoretic impregnation of porous anodic aluminum oxide film by silica nanoparticles. *Colloids Surf A* 415: 187–194. https://doi.org/10.1016/j.colsurfa.2012.09.011
38. He T, Wang YC, Zhang YJ, et al. (2009) Super-hydrophobic surface treatment as corrosion protection for aluminum in seawater. *Corros Sci* 51: 1757–1761. https://doi.org/10.1016/j.corsci.2009.04.027
39. Qin JR, Zhou XR, Curioni M (2023) Investigation of oxide growth during hard anodizing using in-situ and ex-situ EIS measurements. *Surf Coat Technol* 470: 129851. https://doi.org/10.1016/j.surfcoat.2023.129851
40. Dabiri Havigh M, Marcoen K, Wouters B, et al. (2024) Application of operando ORP-EIS for the in-situ monitoring of acid anion incorporation during anodizing. *Electrochim Acta* 493: 144395. https://doi.org/10.1016/j.electacta.2024.144395
41. ASTM International (2023) Standard practice for calculation of corrosion rates and related information from electrochemical measurements. ASTM G102-23. West Conshohocken, PA: ASTM International. https://doi.org/10.1520/G0102-23
42. Zhang C, Zhang DZ, Pan XZ, et al. (2022) Mechanism, application, and research progress of sealing technology for anodic oxide films on aluminum and its alloys. *Electroplat Finish* 41: 1305–1312. https://doi.org/10.19289/j.1004-227x.2022.18.007
43. ASTM International (2011) Standard practice for operating salt spray (fog) apparatus. ASTM B117-11. West Conshohocken, PA: ASTM International. https://doi.org/10.1520/B0117-11
44. Totaro P, Khusid B (2022) Effect of current density ramping on the growth rate and structure of AA2024-T3. *Materials* 15: 3258. https://doi.org/10.3390/ma15093258
45. Yanagimoto H, Saito K, Takahashi H, et al. (2022) Changes in the structure and corrosion protection ability of porous anodic oxide films on pure Al and Al alloys by pore sealing treatment. *Materials* 15: 8544.. https://doi.org/10.3390/ma15238544
46. Kang YX, Li ZI, Yan SF, et al. (2024) Optimization of anodizing conditions and hole sealing treatments for enhanced anti-corrosion properties of magnesium alloys. *Ceram Int* 50: 25667–25678. https://doi.org/10.1016/j.ceramint.2024.04.302
47. Yang EH, Yang RX, Wei W, et al. (2024) Corrosion resistance and antibacterial properties of hydrophobic modified Ce-doped micro-arc oxidation coating. *J Mater Res Technol* 29: 3303–3316. https://doi.org/10.1016/j.jmrt.2024.02.052
48. Robinson KJ, Thissen H (2024) Selecting the best surface analysis method for your materials/samples. *J Vac Sci Technol A* 42: 040801. https://doi.org/10.1116/6.0003576
49. Chen C, Yu M, Zhan ZW, et al. (2023) Effect of pH on the structure and corrosion protection properties of sol-gel coatings. *Corros Sci* 212: 110955. https://doi.org/10.1016/j.corsci.2022.110955
50. Ferraris M, Benelli A, Casalegno V, et al. (2024) Joining and coating of plasma electrolytic oxydated aluminum using a silica preceramic polymer. *Coatings* 14: 757. https://doi.org/10.3390/coatings14060757

51. Catauro M, Blanco I, Fiorentino M, et al. (2022) Synthesis by sol-gel route, chemical, and biological characterization of hybrid material composed by Fe(II)C and poly(ε-caprolactone). *Macromol Symp* 404: 404. https://doi.org/10.1002/masy.202100263
52. Ramasamy SP, Veeraswamy D, Ettiyagounder P, et al. (2023) New insights into method development and characterization of amorphous silica from wheat straw. *Silicon* 15: 5049–5063. https://doi.org/10.1007/s12633-023-02396-5
53. Catauro M, D'Angelo A, Viola V, et al. (2023) Antibacterial and cytotoxic silica-polycaprolactone-chlorogenic acid hybrids by sol-gel route. *Molecules* 28: 3486. https://doi.org/10.3390/molecules28083486
54. Ghaffari Y, Saifuddin M, Kim S, et al. (2022) A novel metal-containing mesoporous silica composite for the decolorization of Rhodamine B: Effect of metal content on structure and performance. *Nanomaterials* 12: 4108. https://doi.org/10.3390/nano12234108
55. Jafari-Tarzanagh Y, Seifzadeh D, Khodayari A, et al. (2022) Active corrosion protection of AA2024 aluminum alloy by sol-gel coating containing inhibitor-loaded mesoporous SBA-15. *Prog Org Coat* 173: 107166. https://doi.org/10.1016/j.porgcoat.2022.107166
56. Mopon ML, Garcia JS, Manguerra DM, et al. (2021) Corrosion behavior of AA 1100 anodized in gallic-sulfuric acid solution. *Coatings* 11: 405. https://doi.org/10.3390/coatings11040405
57. Shao LL, Li HT, Jiang BL, et al. (2018) A comparative study of corrosion behavior of hard anodized and micro-arc oxidation coatings on 7050 aluminum alloy. *Metals* 8: 165. https://doi.org/10.3390/met8030165
58. Hirschorn B, Orazem ME, Tribollet B, et al. (2010) Determination of effective capacitance and film thickness from constant-phase-element parameters. *Electrochim Acta* 55: 6218–6227. https://doi.org/10.1016/j.electacta.2009.10.065
59. Cabral-Miramontes J, Cabral-Miramontes N, Nieves-Mendoza D, et al. (2024) Anodizing of AA2024 aluminum–copper alloy in citric-sulfuric acid solution: Effect of current density on corrosion resistance. *Coatings* 14: 816. https://doi.org/10.3390/coatings14070816
60. Zeng DP, Liu ZY, Bai S, et al. (2019) Influence of sealing treatment on the corrosion resistance of PEO coated Al-Zn-Mg-Cu alloy in various environments. *Coatings* 9: 867. https://doi.org/10.3390/coatings9120867
61. Singh H, Xiong Y, Rani E, et al. (2022) Unveiling nano-scaled chemical inhomogeneity impacts on corrosion of Ce-modified 2507 super-duplex stainless steels. *npj Mater Degrad* 6: 54. https://doi.org/10.1038/s41529-022-00263-z
62. Zheng SX, Li JH (2010) Inorganic–organic sol gel hybrid coatings for corrosion protection of metals. *J Sol-Gel Sci Technol* 54: 174–187. https://doi.org/10.1007/s10971-010-2173-1
63. Xu XC, Liu DX, Zhang XH, et al. (2020) Effects of ultrasonic surface rolling on the localized corrosion behavior of 7B50-T7751 aluminum alloy. *Materials* 13: 738. https://doi.org/10.3390/ma13030738
64. Akbarzadeh S, Paint Y, Olivier MG (2023) A comparative study of different sol-gel coatings for sealing the plasma electrolytic oxidation (PEO) layer on AA2024 alloy. *Electrochim Acta* 443: 141930. https://doi.org/10.1016/j.electacta.2023.141930
65. Usman BJ, Scenini F, Curioni M (2020) The effect of exposure conditions on performance evaluation of post-treated anodic oxides on an aerospace aluminium alloy: Comparison between salt spray and immersion testing. *Surf Coat Technol* 399: 126157. https://doi.org/10.1016/j.surfcoat.2020.126157

66. Wang C, Sun SN, Ling YH, et al. (2024) The corrosion resistance of tartaric-sulfuric acid anodic films on the 2024 Al alloy sealed using different methods. *Coatings* 14: 733. https://doi.org/10.3390/coatings14060733

AIMS Press